On the rotation of a Savonius turbine at low Reynolds numbers subject to Kolmogorov cascade of turbulence

Shūji Ōtomo (大友衆示),[1,2,*] Yuji Tasaka (田坂裕司),[2,†] Petr Denissenko,[3,‡] and Yuichi Murai (村井祐一)[2,§]

[1] *Graduate School of Engineering, University of Agriculture and Technology, Tokyo 184-8588, Japan*
[2] *Laboratory for Flow Control (LFC), Faculty of Engineering, Hokkaido University, N13W8, Sapporo 060-8628, Japan*
[3] *School of Engineering, University of Warwick, Coventry CV4 7AL, UK*

With an increasing demand for small energy generation in urban areas, small-scale Savonius wind turbines are growing their share rapidly. In such an environment, Savonius turbines are exposed to low mean velocity with highly turbulent flows made by complex geographies. Here we report the flow-induced rotation of a Savonius turbine in a highly turbulent flow (18% turbulence intensity). The high turbulence is realised by using the far-field of an open-jet. Compared to low turbulence inflow (1% turbulence intensity), the turbine rotates 4% faster in high turbulence since the torque/power increases with turbulence intensity. The wake measurement by hot-wire anemometry and particle image velocimetry reveals the suppression of vortex shedding in high turbulence. In addition, a newly developed semi-empirical low-order model, which can include the effect of turbulence intensity and integral length scale, also confirms high turbulence intensity contributes to the rotation of the turbine. These results will boost more installation of small Savonius turbines in urban areas in the future.

I. INTRODUCTION

Clean power generation is one of the primary targets of sustainable development goals. Wind turbines are expected to play a significant role in replacing fossil fuel-based power generation. Large-scale propeller-type horizontal axis wind turbines (HAWTs) have been playing a primary role in responding to this demand. On the other hand, in recent years, small-scale power generation in urban areas has been expected to increase as a means of on-site electrical production systems. For this purpose, vertical axis wind turbines (VAWTs) are superior to HAWTs since VAWTs are known to be more robust in urban wind conditions characterised by low mean velocity and high turbulence intensity than atmospheric winds due to complex terrains [1–3]. VAWTs are generally categorised into two kinds, one is lift driven such as Darrius wind turbines, and the other is drag driven such as Savonius turbines [4]. The primary advantage of VAWTs is their omnidirectional wind acceptance. In addition to this, the Savonius wind turbine has unique abilities over other kinds of wind turbines such as quiet operation, low cut-in speed, harmoniousness with urban landscapes, and simple construction. Because of these advantages, Savonius wind turbines are often introduced in urban areas. Wind flows in urban areas have low mean velocities and higher turbulence intensity than atmospheric winds due to their complex terrains. Zou *et al.* [5] measured the turbulence characteristics of urban wind at a pedestrian level and found the turbulence intensity was 30 - 40% and the integral lengthscale was 3 - 6 m. Conventional-sized Savonius turbines in urban areas are, for example, used for a street lighting system [6, 7] and on-site power generation system for buildings [8–10]. Under such environments, Savonius turbines operate typically at the diameter-based Reynolds number Re of $\mathcal{O}(10^5)$.

In recent years, more downsized Savonius turbines have been developed. It is known that the performance of Savonius turbines with helically twisted blades decreases with decreasing Reynolds numbers [11], whereas conventional (non-twisted) Savonius turbines show robustness in power acquisition at lower Reynolds numbers [12, 13]. This is because the helical blade surface causes negative pressure due to the streamlined curvature that contributes to the additional torque generation. One example of conventional Savonius turbines at low Reynolds numbers is a wind energy harvesting device called *aeroleaf* [14], which has the shape of a tree consisting of a cluster of conventional (non-twisted) Savonius turbines, developed for various applications such as providing street lights, WiFi hotspot, and mobile devices charging. This wind energy harvester has a size of 10 m and consists of more than 30 Savonius turbines which operate at $Re = \mathcal{O}(10^4)$. On a rather smaller scale, Wang and Yeung [13] investigated a micro-scale conventional Savonius turbine at $Re = 1500$ as its application for powering wireless sensor nodes. They found that the micro-scale Savonius turbine exhibited the maximum power coefficient of 0.18, which is approximately the same

* Author to whom correspondence should be addressed; otomo@go.tuat.ac.jp
† tasaka@eng.hokudai.ac.jp
‡ p.denissenko@warwick.ac.uk
§ murai@eng.hokudai.ac.jp

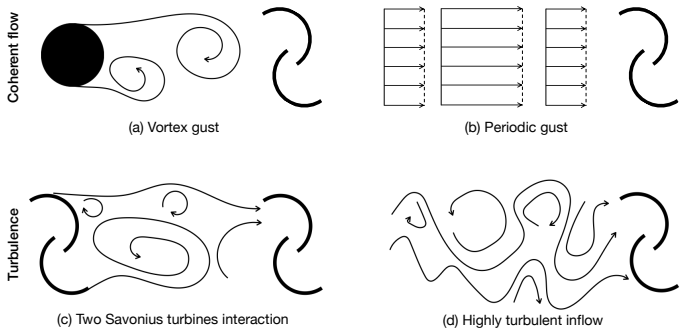

FIG. 1: Classification of flow disturbances: (a) vortex gust, (b) periodic gust, (c) Two turbines interaction, and (d) highly turbulent inflow.

as the power coefficient at a much higher Reynolds number $Re = 80000$. Their study shows that Savonius turbines have the ability to operate at very low Re. For those small-scale Savonius turbines, both their size and rotational frequency are exposed in the inertial subrange in the energy spectrum of the inflow turbulent wind. In such conditions, other lift-driven wind turbines exhibit poor performances as the lift coefficient decreases with Reynolds numbers. For these reasons, Savonius turbines are more suitable for lower Reynolds numbers. Therefore in this paper, we perform experiments at $Re = \mathcal{O}(10^4)$.

Figure 1 illustrates the classification of inflow disturbances. The flow disturbances are first categorised into a coherent flow and turbulence. The coherent flow is further classified into: (a) vortex gust such as Kármán vortex shedding from an upstream cylinder interacting with the turbine when the vortex shedding frequency matches with the rotational frequency of the turbine, and (b) periodic streamwise gust whose frequency improves the power output of the turbine. Turbulence is classified into (c) two Savonius turbines interaction and (d) highly turbulent inflow. For (c) two Savonius turbines interaction, periodic velocity fluctuation from the upstream turbine affects the performance of the turbine downstream. Shigetomi *et al.* [15] found an optimal arrangement of the two turbines that improves the power output than the single turbine. Highly turbulent inflow that contains a wide wave spectrum of kinetic energy also affects the turbine characteristics, which is the focus of the present study.

There are a number of researches that investigated the effect of freestream turbulence on horizontal axis propeller type turbines, for example, in [16–23]. There have been also several studies to understand the effect of freestream turbulence on Savonius turbines. Wekesa *et al.* [18] tested a two-staged and three-bladed Savonius turbine in turbulence with turbulence intensity between 9% and 14%. They observed turbine's efficiency increased in turbulence when $Re < 340000$. In contrast, Loganathan *et al.* [24] investigated the effect of turbulence on a multi-bladed Savonius turbine (24 - 40 blades) at $Re = 230000$ and confirmed that the power output decreased with turbulence intensity. Aliferis *et al.* [25] also observed the decrease in efficiency with increasing turbulence intensity up to 5.7% for a twisted Savonius turbine at Re of $\mathcal{O}(10^5)$. These previous studies suggest that the Savonius turbine may have a better performance in turbulence when the Reynolds number is low. In this paper, we investigate the effect of freestream turbulence with turbulence intensity of 18% at lower Reynolds numbers of $\mathcal{O}(10^4)$.

The conventional Savonius turbine sheds coherent vortical structures in the wake in the flow with low turbulence intensity [13, 15, 26–28]. These detached vortices, which contain kinetic energy, are advected downstream, resulting in energy loss for the turbine. For static bluff-bodies in a turbulent inflow, significant suppression of the vortex shedding was reported [29–32]. This attenuated vortex shedding is related to the alternation of the separation point on the body surface due to turbulence. For a rotating Savonius turbine, such vortex shedding attenuation has not been clarified yet.

Figure 2 illustrates the possible turbulent flow spectrum and corresponding turbine sizes. When the turbine is in the integral scales of the turbulence spectrum (a), the turbine-turbulence interaction depends on the on-site condition, which exhibits complex characteristics influenced by intrinsic coherent flow structure. In the inertial subrange (b), where Kolmogorov's -5/3 law stands, the kinetic energy of the flow is always transferred to the finer scales as indicated by an arrow in the figure. Here we are interested in the effect of freestream turbulence on the Savonius turbine when its size or rotational speed is inside the inertial subrange where the energy cascade occurs. In real urban wind conditions, Savonius turbines typically have a diameter of $10^{-1} - 10^{0}$ m [33] rotating at $f_{\mathrm{rot}} = 10^{-1} - 10^{1}$ Hz and urban wind

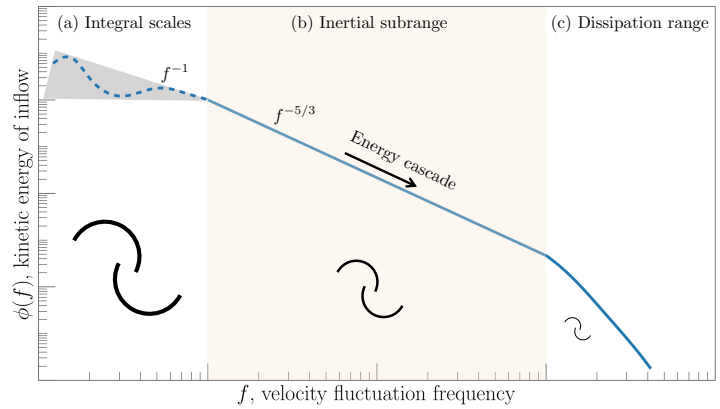

FIG. 2: The scale of a Savonius turbine in turbulent flow spectrum: (a) integral scale has a spectrum dependent on flow configuration and energy transfers in two-way between small and large scales where coherent flow structures affect the rotation of the turbine, (b) inertial subrange has the universality of turbulent flow property following Kolmogorov's -5/3 law and one-way energy cascade occurs from large to small scales, and (c) in viscous scale, flow fluctuation is attenuated by viscous energy dissipation to be converted gradually into thermal energy. In this study, the Savonius turbine's scale is in (b) inertial subrange. Note that this figure is conceptual and in reality the Savonius turbine having the size of the integral scale and Kolmogorov scale is unrealistic, whilst the Savonius turbine having the same size as the integral lengthscale is possible in wind tunnel experiments.

has the inertial subrange at $f = 10^{-2} - 10^{1}$ Hz [5]. Therefore, Savonius turbines are expected to rotate inside the inertial subrange of the inflow wind.

The aim of this study is to investigate the Savonius turbine rotation and its wake in highly turbulent freestream conditions following Kolmogorov's energy cascade at low Reynolds numbers ($Re = \mathcal{O}(10^4)$). To accomplish this aim, we place the Savonius turbine in the far-field of an open-jet. We perform the rotational speed measurement and wake measurement by particle image velocimetry (PIV) and hot-wire anemometry (HWA). In addition to this, we develop a semi-empirical low-order model, which includes the effect of turbulence intensity and integral length scale, to predict the flow-induced rotation of the turbine. The rest of the paper consists as follows. Section II provides the flow characteristics of the jet. Section III describes the details of the free-rotation measurement, PIV, and HWA. Section IV provides the low-order semi-empirical model to predict the flow-induced rotation of the Savonius turbine. In Section V, the results of the free-rotation measurement, the low-order model, and the wake measurement are presented. Finally, conclusions are drawn in Section VI.

II. FLOW CHARACTERISTICS OF AN OPEN-JET

In this section, we provide the turbulence characteristics of the open-jet used in the entire experiment. Unlike conventional methods for turbulence generations such as a turbulence grid, the far-field of the open-square-jet is used. Although it is known that the flow in the far-field of turbulent jets has high turbulence intensity close to 20 %, nearly isotropic turbulence, and a wide inertial subrange with Kolmogorov's -5/3 law [34–37], it is uncommon to use the far-field of open-jet to study the freestream turbulence-body interaction. Thereby, in this section, we compare the turbulence characteristics of the far-field jet with other conventional turbulence generating methods in literature.

The open-square-jet is comprised of a fan, a duct, an expansion section, a straighter mesh, a contraction section, and a square nozzle. The jet outlet has a square nozzle of $B = 0.35$ m, and the center of the nozzle is located 1.42 m above the floor. The Cartesian coordinates X, Y, and Z axes are in streamwise, vertically upwards, and spanwise directions, respectively with the origin located at the centre of the jet nozzle outlet as depicted in Fig. 3. The flow development of the open-square-jet is also illustrated schematically in the figure.

Static hot-wire anemometry (HWA) with the constant temperature method is used to measure the instantaneous streamwise velocity component. The hot-wire probe is comprised of a single tungsten wire of 5 μm in diameter and

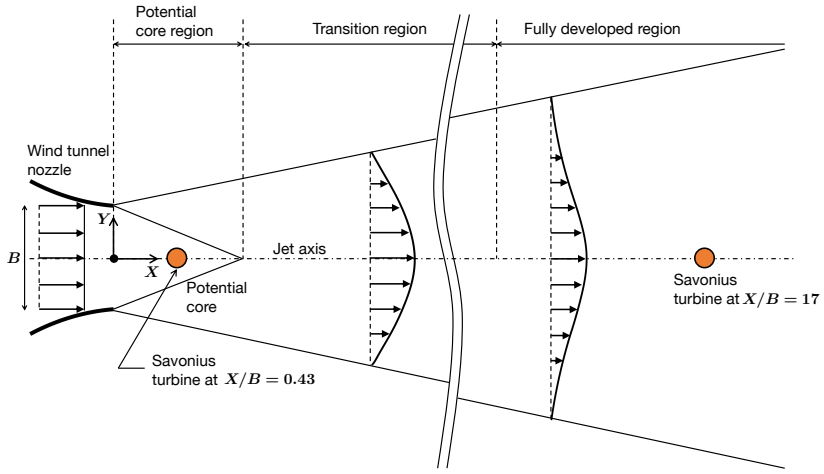

FIG. 3: Schematics of the flow development along the open-jet axis.

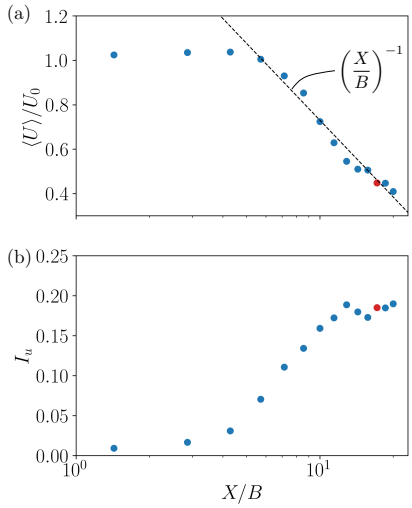

FIG. 4: (a) Mean velocity decay $\langle U\rangle/U_0$ and (b) turbulence intensity development I_u along the jet axis. The red markers denote the values at which the Savonius turbine is placed ($X/B = 17$).

2 mm in length. Signals are recorded at a sampling frequency of 1 kHz for the length of 2^{17} points, which correspond to the recording time of approximately 131 s. The streamwise velocity component is measured at 16 locations between $0 \le x \le 7.5$ m ($0 \le X/B \le 21.4$) at 0.5 m interval along the center-line. HWA is calibrated at the center of the nozzle exit where the relation between the exit velocity U_0 and the fan rotation frequency is investigated by a pitot tube.

The mean streamwise velocity decay $\langle U\rangle/U_0$ and turbulence intensity $I_u = u'/\langle U\rangle$ are shown in Fig. 4. Here $\langle U\rangle$ is the mean freestream velocity and u is the velocity fluctuation. The angle brackets $\langle\cdot\rangle$ denote the mean value and the superscript $'$ denotes the root-mean-square value (e.g. $u' = \sqrt{\langle u^2\rangle}$). The figure shows that the region $X/B < 3$ is

TABLE I: Comparison of turbulence characteristics with other turbulence generating methods.

Experiment and reference	$\langle U\rangle$ [m/s]	I_u [%]	η [mm]	λ [mm]	L [mm]	ε [m^2/s^3]	Re_λ	Applications
Turbulence grid by mesh								
Kistler and Vrebalovich [44]	61	1.97	0.047	2.4	47.8	16.2	669	-
Aliferis et al. [25]	13.9	5.7	-	-	-	-	-	Twisted Savonius turbine
Turbulence grid with jet injection								
Gad-el Hak and Corrsin [47]	8.16	3.18	0.39	9.45	134.7	0.156	160	-
Active grid								
Makita [48]	5.0	16.4	0.21	8.2	197	1.72	387	-
Rockel *et al.* [19]	6	15.9	-	-	-	-	-	HAWT
Talavera and Shu [20]	13	8	-	-	-	-	-	HAWT
Gambuzza and Ganapathisubramani [23]	8	11.6	-	-	1880	-	-	HAWT
Vinod and Banerjee [22]	0.82	13.9	-	-	110	-	-	Tidal turbine
Atmospheric turbulence								
Praskovsky and Oncley [49]	7.08	14.1	0.64	106	81000	0.0201	7100	-
Open-jet far-field								
Present study	2.7	18.5	0.44	19.3	335	0.0720	486	Savonius turbine

the potential core region where the exit velocity is nearly constant and turbulence intensity is low. In the transition region $X/B > 3$, the mean streamwise velocity decays proportionally to $(X/B)^{-1}$. Turbulence intensity I_u increases with X/B until it reaches $X/B \approx 13$, where it asymptotes to $I_u \approx 0.18$ in the far-field. Thereby we select $X/B = 17$ for testing the Savonius turbine in a high turbulence condition. At $X/B = 17$, the effect of the mean velocity profile of the jet on the Savonius turbine is negligible since the mean velocity at the tip of the Savonius turbine ($Y = 29$ mm) is estimated to be $0.998\langle U\rangle$ by the empirical model [38–40]. Hence it is deemed that the turbine receives almost the same mean momentum.

The Kolmogorov scale $\eta = (\nu^3/\varepsilon)^{1/4}$ is estimated from dissipation rate with locally isotropic assumption $\varepsilon = 15\nu\langle(\partial u/\partial x)^2\rangle$. The derivative is determined through a modified version of Taylor's frozen hypothesis, $\partial u/\partial x = -(\langle U\rangle + u)^{-1}\partial u/\partial t$ as adopted in previous studies on turbulent jets [36, 41, 42]. The Taylor microscale is computed by $\lambda = \langle u^2\rangle^{1/2}/\langle(\partial u/\partial x)^2\rangle^{1/2}$. The integral length scale L is estimated based on Taylor's frozen hypothesis as

$$L = \langle U\rangle \int_0^{\tau_L} \frac{\langle u(t)u(t+\tau)\rangle}{\langle u^2\rangle} \mathrm{d}\tau, \tag{1}$$

where τ_L is the first zero-crossing location of the auto-correlation function (integrand) and τ is the delay. The integral length scale is $L = 335$ mm at $X/B = 17$. This corresponds to $L/D = 5.78$, where D is the diameter of the Savonius turbine used in the experiment.

A number of researchers have attempted to generate large-scale turbulence with high turbulence intensity, high turbulence Reynolds number Re_λ, and a wide inertial subrange since Batchelor [43] stated that the existence of the inertial subrange is clearly unlikely to be obtained in laboratory wind tunnels. A classical method is to use a turbulence grid. Kistler and Vrebalovich [44] measured the characteristics of turbulence generated by a square-mesh turbulence grid in a large adjustable-pressure wind tunnel. They obtained a high turbulence Reynolds number over 600 and succeeded in obtaining a wide inertial subrange over 10^2 in the wavelength for the first time. This classical method is simple and therefore still popular in researching the effect of turbulence on wind turbines [16, 18, 24, 25, 45, 46]. Gad-el-Hak and Corrsin [47] applied jet injection to a grid and obtained a larger scale of turbulence ($L = 134.7$ mm) than the conventional grid turbulence when the jet was injected in a counter-flow direction. However, no clear inertial subrange was observed in the energy spectrum. Makita [48] is a pioneer of the active grid generated turbulence. He succeeded in obtaining a large-scale turbulence with $u'/\langle U\rangle = 16.4\%$ and turbulent Reynolds number based on Taylor's microscale $Re_\lambda = \langle U\rangle\lambda/\nu = 387$ by oscillating agitator wings attached to turbulence grids. Nowadays, this method has become popular in wind/tidal turbine research in turbulence [19, 20, 22, 23].

The turbulence characteristics of grid-generated turbulence are compared with those of our open-jet in Table I. The turbulence characteristics of atmospheric turbulence (7 m above the ground) measured by Praskovsky and Oncley [49] are also added in the table.

Figure 5 shows the power spectral density (PSD) $\phi(f)$ of the streamwise velocity fluctuation u measured $17B$ downstream the nozzle outlet. PSD of 2^{17} points (corresponding to approximately 131 seconds) is computed using Welch's method [50] applying a Hanning window of 2^{11} points (corresponding to approximately 2 seconds) with a 50 % overlap. The figure shows a wide inertial subrange in which a clear Kolmogorov's $-5/3$ law is present in the frequency band between approximately 1 Hz and 100 Hz. The shaded region indicates the mean rotational speed

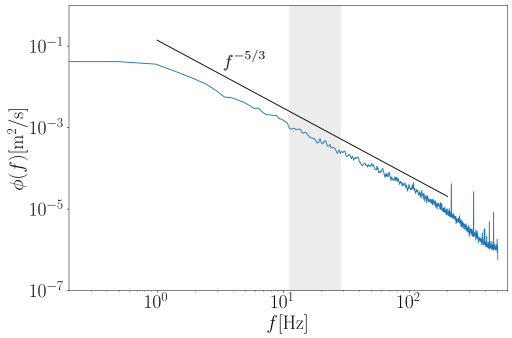

FIG. 5: Power spectral density (PSD) of velocity fluctuation in the far field of the open-jet wind tunnel outlet $17B$ downstream the nozzle outlet. The shaded region, which is the measured rotational frequency of the Savonius turbine, lies within the inertial subrange where the energy cascade occurs.

of the Savonius turbine at the freestream velocity ranging $2.5 < U < 6$ m s^{-1} and it is clear that it lies within the inertial subrange.

III. MEASUREMENT TARGET

Experiments are performed at the wind tunnel facility of the Laboratory for Flow Control at Hokkaido University. As described in the previous section, the open-jet wind tunnel with 0.35 m × 0.35 m square nozzle is used. A small Savonius turbine model with the diameter $D = 58$ mm is used to explore the flow-induced rotation at low Reynolds numbers for free-rotation conditions (i.e. only friction force from bearings acts on the turbine). Fig. 6 shows the cross-section of the Savonius turbine model used in the experiment. The turbine consists of two half-cylindrical blades with an overlap distance $d_o = 8$ mm, one end plate on the bottom, and a shaft. The blades are made of acrylic resin and painted in black to minimise light reflection. The half-cylindrical blades have a radius of $a = 16$ mm, a height of $H = 80$ mm, and a thickness of $\delta = 0.5$ mm. The aspect ratio of the turbine and the overlap ratio are $H/D = 1.38$ and $d_o/D = 0.14$, which are common in Savonius turbine research [33, 51].

The turbine is placed at $X/B = 0.43$ as a low turbulence intensity flow condition (LT flow) and $X/B = 17$ as a high turbulence intensity flow condition (HT flow). In both cases, the mid-height of the turbine is placed along the centre line of the open-square-jet outlet. The experimental condition is summarised in Table II.

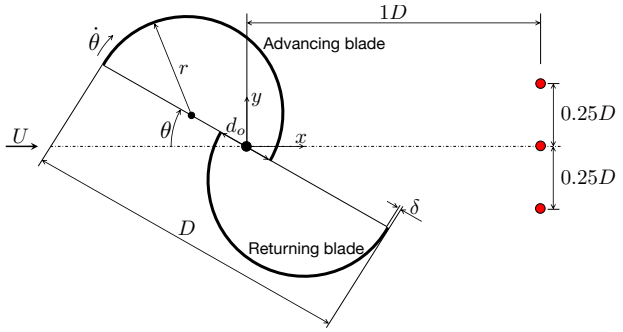

FIG. 6: Cross section of Savonius turbine and definition of geometric parameters. Red markers indicate the locations of hot-wires for the wake velocity measurement.

TABLE II: Experimental conditions.

Turbine diameter D [mm]	58
Blade curvature radius a [mm]	16
Overlap distance d_o [mm]	8
Turbine height H [mm]	80
Reynolds number Re	9600
Turbulence intensity I_u [%]	1 and 18.5
Integral length scale L/D	5.8

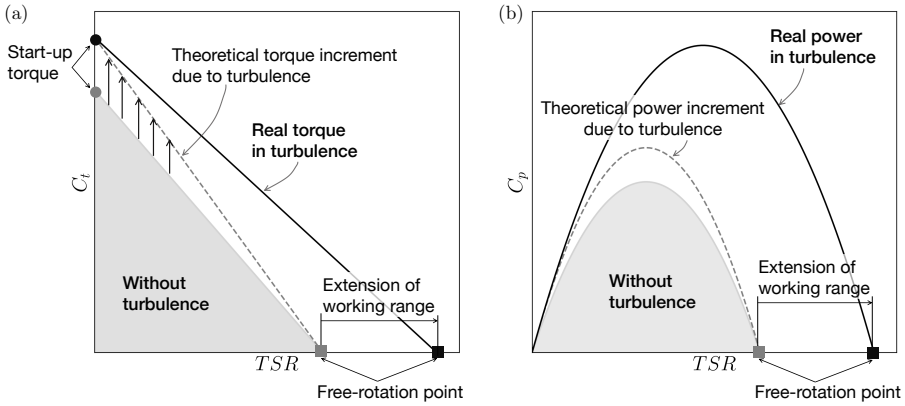

FIG. 7: Estimated contribution of turbulence to Savonius turbine performance: (a) torque coefficient C_t which theory explains the increment due to turbulence but no theory gives the extension of the working range in TSR, and (b) power coefficient C_p largely expands if the free rotation point shifts (square markers) to higher TSR. This is the rationale behind measuring the free rotational speed. Note that the curves are exaggerated to make the difference clear.

A. Rotational speed measurement

For the rotational speed measurements, the mean freestream velocity is varied such that $\langle U\rangle \in \{2.5, 4, 5, 6\}$ m s^{-1}, which correspond to the diameter-based Reynolds numbers of $Re \in \{0.96, 1.5, 1.9, 2.3\} \times 10^4$. The rotational speed of the Savonius turbine $\dot{\theta}$ is recorded for 240 s by a laser tachometer at every 1 s. The Savonius turbine is driven mainly by drag and typically its torque decreases linearly with the tip-speed ratio $TSR = D\dot{\theta}/(2U)$. This is the reason why the power coefficient curve is parabolic. Fig. 7 illustrates our target in this measurement. Our question is how the conventional Savonius turbine is influenced by turbulence. Theoretically, the time-averaged torque of the turbine increases with velocity fluctuation. The torque of the turbine is proportional to $U^2 = (\langle U\rangle + u)^2$,

$$T \propto (\langle U\rangle + u)^2 = \langle U\rangle^2 + 2\langle U\rangle u + u^2. \tag{2}$$

By taking the time average,

$$\langle T\rangle \propto \langle U\rangle^2\left(1 + \frac{\langle u^2\rangle}{\langle U\rangle^2}\right) = \langle U\rangle^2\big(1 + I_u^2\big), \tag{3}$$

which means that the turbulence intensity increases the time-average torque. In a similar manner, the power output W of the turbine is proportional to $U^3 = (\langle U\rangle + u)^3$,

$$W \propto (\langle U\rangle + u)^3 = \left(\langle U\rangle^3 + 3\langle U\rangle^2 u + 3\langle U\rangle u^2 + u^3\right), \tag{4}$$

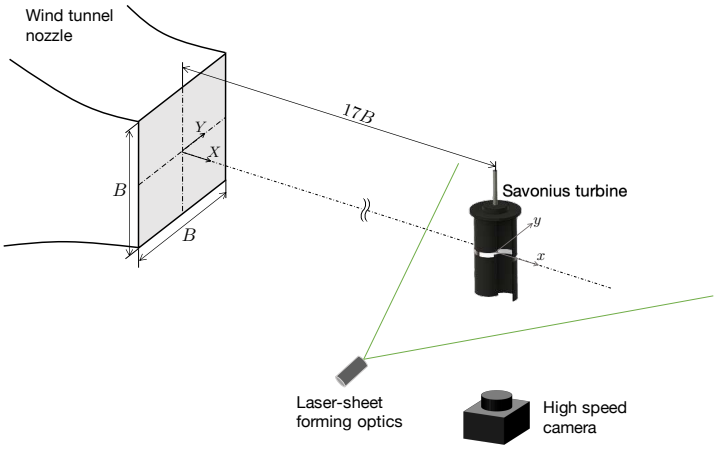

FIG. 8: Experimental setup for PIV measurement.

By taking the time average, we obtain

$$\langle W\rangle \propto \langle U\rangle^3\left(1+3\frac{\langle u^2\rangle}{\langle U\rangle^2}\right) = \langle U\rangle^3(1+3I_u^2). \tag{5}$$

The equation tells us that the power increases by $3I_u^2$. This relation between the time-averaged power and turbulence intensity is also reported in, for example, [15, 52–55]. In Fig. 7, This trend is illustrated by a grey solid line to a grey dashed line in (a) the torque coefficient C_t and (b) the power coefficient C_p, respectively. On the other hand, TSR at the free rotation condition, i.e. the rotational speed of the turbine in the unloaded state (no generator is connected), can be hardly estimated in theory. It is determined by the balance between positive and negative instantaneous torque acting on the blades during its rotation. By measuring the free rotational speed in high turbulence, we estimate the contribution of turbulence to the extension of the energy harvestable range in TSR. To this end, the turbine must be operated as autorotation, i.e. flow-induced rotation. Black solid lines in Fig. 7 depict the significant improvement of the turbine performance as the free rotational speed shifts higher (grey and black square markers in Fig. 7) due to the effect of turbulence. In this context, we compare the free rotational speed in the LT and HT flows.

B. Wake measurement

The Reynolds number is set at $Re = 0.96\times10^4$ for the wake measurements by hot-wire anemometry (HWA) and particle image velocimetry (PIV). Time-resolved particle image velocimetry is performed to measure the velocity in the wake of the turbine. The schematic drawing of the PIV experiment smoke flow visualisation setup is shown in Fig. 8. Smoke made of oil mist (10 μm average diameter) is illuminated by a laser (Nd:YAG, 532 nm) emitted horizontally on the plane of half the turbine height. A high-speed camera (Photron, FASTCAM Mini AX50) with 1024×1024 pix resolution captures 5000 images at 1000 Hz. Adaptive multi-pass cross-correlation is employed to compute velocity vectors, with a final interrogation window of 32×32 pix, and an overlap of 67%, yielding a physical resolution of 2.8 mm or $0.048D$. Outliers are detected by the universal outlier detection [56] and interpolated by Laplace equation interpolation algorithm [57, 58]. Phase-averaged velocity fields are obtained for 62 periods assuming that half a revolution makes one cycle.

HWA is conducted in order to obtain time-resolved measurements of the streamwise component of inflow and wake velocity. Signals are recorded at 1k Hz for the length of 2^{17} points, which correspond to the recording time of approximately 131 s. As the turbine rotates at $f_{\rm rot} = 10.98$ Hz, the turbine rotates approximately 1400 times during the measurement. The inflow velocity is measured $2D$ upstream at $(x/D, y/D) = (-2, 0)$. Wake velocity is measured at three different positions $1D$ downstream, on the centre line at $(x/D, y/D) = (1, 0)$, behind the advancing blade at $(x/D, y/D) = (1, 0.25)$, and behind the returning blade at $(x/D, y/D) = (1, -0.25)$, respectively. These three

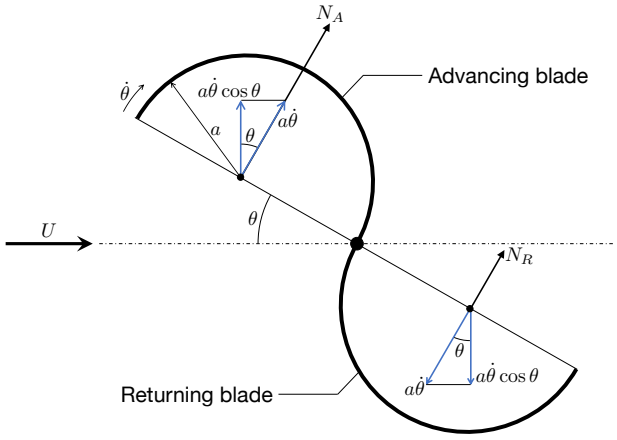

FIG. 9: Normal forces and the characteristic blade velocities on Savonius turbine without an overlap distance. N_A and N_R are normal forces acting on the advancing blade and returning blade, respectively.

locations for the wake velocity measurement are respectively referred to as 'centre', 'advance', and 'return' later in the result section (Fig. 17).

IV. SEMI-EMPIRICAL LOW-ORDER MODEL

In this section, we present a semi-empirical low-order model to predict the flow-induced rotation of a Savonius turbine under the free-rotation condition. In this paper, we focus on two effects of turbulence on the turbine's rotation. One is due to the attenuated vortex shedding, and the other is the turbulent kinetic energy of the inflow wind. The first is investigated by the PIV and HWA measurements in the wake of the turbine. Therefore this section provides a semi-empirical model, which includes the influence of inflow unsteadiness obeying Kolmogorov cascade on the Savonius turbine's rotation.

The main aim of presenting a low-order model is to better understand the effect of inflow unsteadiness on the turbine rotation, rather than to provide a universal model which can accurately predict the turbine rotation. For this purpose, we develop a simple semi-empirical low-order model, in which only Kolmogorov cascade is considered as the characteristics of turbulence. Therefore the effect of vortex formation is not included.

The governing equation of the rotational speed of the Savonius turbine ω is expressed as

$$I\frac{\mathrm{d}\omega}{\mathrm{d}t} = T_\mathrm{G} - T_\mathrm{F} \tag{6}$$

where I, t, T_G, and T_F are the moment of inertia, time, unsteady aerodynamic torque acting on the turbine, and friction torque of a bearing, respectively. For simplicity, we assume that normal force contributes to the turbine's rotation and that the turbine does not have an overlap distance as shown in Fig. 9. The aerodynamic interaction between advancing and returning blades and the effect of vortex shedding are neglected. As shown in Fig. 9, N_A and N_R are the quasi-steady normal forces respectively acting on the advancing blade and returning blade. The moment arm of normal forces has the length of the rotor curvature radius a located at the mid-chord of the blade. The aerodynamic torque T_G acting on the turbine, and the friction torque T_F by bearing with inner diameter d_B and friction coefficient μ are expressed as,

$$T_\mathrm{G} = a(N_\mathrm{A} - N_\mathrm{R}), \tag{7}$$

$$T_\mathrm{F} = \frac{1}{2}\mu d_\mathrm{B}(N_\mathrm{A} + N_\mathrm{R}), \tag{8}$$

where normal forces are written as

$$N_\mathrm{A} = \frac{1}{2}\rho U^2 S C_\mathrm{NA}(\theta_\mathrm{eff}) \text{ and } N_\mathrm{R} = \frac{1}{2}\rho U^2 S C_\mathrm{NR}(\theta_\mathrm{eff}), \tag{9}$$

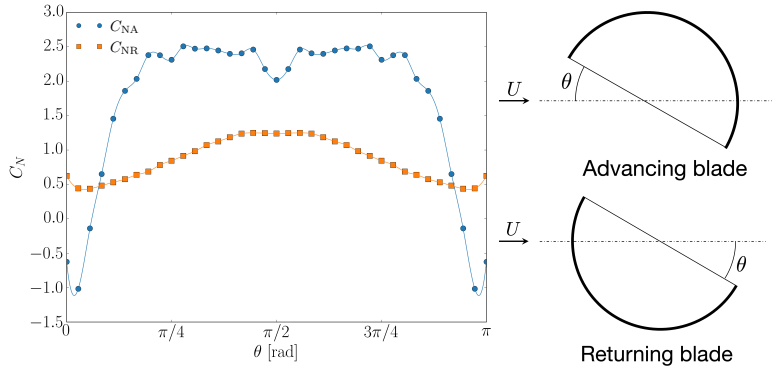

FIG. 10: Normal force coefficients of the advancing and returning blades with respect to the angle of attack θ. Data points are taken from Kyozuka [59] and solid lines show cubic spline interpolation.

with ρ as the density of the fluid. $S = 2aH$ is the reference area of the blade. C_{NA} and C_{NR} are quasi-steady normal force coefficients of the advancing blade and the returning blade, respectively. θ_{eff} is the effective angle of attack. In the computation, we use those normal force coefficients of a static semi-circular cylinder provided in Kyozuka [59] as plotted in Fig. 10. In their measurement, the blade has end-plates on both ends of the blade and forces are measured at $Re = \mathcal{O}(10^5)$ at the angle of attack of $0° \leq \theta \leq 180°$ at every 5°. In reality, forces acting on turbine blades are influenced by the other blade due to the flow interaction between turbine blades, but this interaction is not considered in this model analysis. Hence, for simplicity, we assume two blades are separated from one another (i.e. two blades with the phase difference of π are rotating independently.). The unsteady effect is taken into account by introducing the effective angle of attack θ_{eff}, which is the sum of the geometric angle of attack and the induced angle of attack due to turbine rotation: $\theta_{\mathrm{eff}} = \theta + \theta_{\mathrm{i}}$. As shown in Fig. 9, the stream-normal velocity of the blades due to their rotation is $a\dot{\theta}\cos\theta$ and thereby the induced angle of attack θ_{i} is defined by

$$\theta_{\mathrm{i}} = \begin{cases} -\arctan\left(\dfrac{a\dot{\theta}\cos\theta}{U}\right) & \text{(advancing blade)} \\ \arctan\left(\dfrac{a\dot{\theta}\cos\theta}{U}\right) & \text{(returning blade)} \end{cases} \tag{10}$$

One-dimensional turbulent inflow velocity is synthetically generated by Shinozuka method [60, 61], which simulates the wind velocity time series as

$$U = \sqrt{2\Delta f}\sum_{i=1}^{N}\sqrt{\phi(f)}\sin(2\pi f_i t + \psi_i), \tag{11}$$

where Δf is the frequency spacing, N the number of f_i components, $\phi(f)$ the turbulence spectrum model, and ψ is the phase angle, which is a uniformly distributed random variable between 0 and 2π. Here we assume that the turbulence is spatially uniform. Scarlett and Viola [62] successfully evaluated the unsteady loads acting on tidal turbine blades using the synthetically generated one-dimensional turbulence. Amongst various turbulence spectrum models, von Kármán model spectrum [63] and Kaimal spectrum [64] are frequently used [65, 66]. We choose von Kármán model spectrum as it is based on the assumption that the turbulence is homogeneous and isotropic. In addition, von Kármán spectrum fits well for turbulence in wind tunnels and hence it is often used for consistency with analytical expressions for correlations [66].

$$\phi(f) = \frac{4u'^2(L/\langle U\rangle)}{[1 + 70.8(fL/\langle U\rangle)^2]^{5/6}}. \tag{12}$$

Fig. 11 shows the von Kármán spectrum generated for $\langle U\rangle = 2.5$ m/s, $u'/\langle U\rangle = 0.18$, and $L = 0.335$ m, representing the PSD obtained in the far-field of the open-jet in our experiment very well.

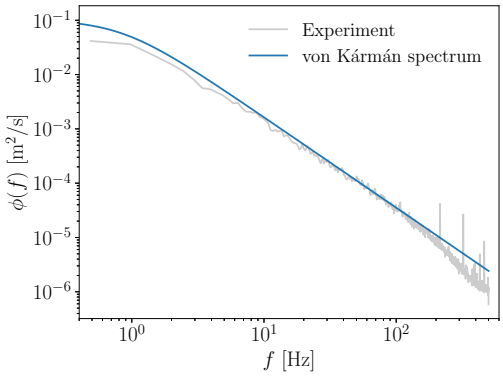

FIG. 11: von Kármán model spectrum (Eq. 12) for $\langle U \rangle = 2.5$ m/s, $u'/\langle U \rangle = 0.18$, and $L = 0.335$ m. The PSD obtained by experiment at $X/B = 17$ is plotted in grey.

TABLE III: Geometric parameters of the Savonius turbine and calculation conditions to solve Eq. 6.

Turbine height H [mm]	80
Turbine blade curvature radius a [mm]	16
Moment of inertia I [kg·m^2]	1×10^{-6}
Friction coefficient of bearing μ [-]	0.0015
Inner diameter of bearing d_B [m]	0.004
Density of air ρ [kg/m^3]	1.2
Initial rotational speed ω_0 [rad/s]	$0.2\langle U \rangle / R$
Time increment Δt [s]	0.01
Maximum time t_max [s]	500

The ordinary differential equation (Eq. 6) is solved using the implicit method based on multi-step variable order (1st to 5th order) backward differentiation formulas. As Table III summarises, the geometric parameters of the Savonius turbine are similar to our experimental conditions. The moment of inertia of blades I is estimated by approximating the blades as an acrylic flat plate. Conditions for computations are also listed in Table III.

V. RESULTS

A. Flow-induced rotation

The mean tip-speed ratio $\langle TSR \rangle$ for different Reynolds numbers Re are compared between the experiment and semi-empirical model in Fig. 12. Overall, the model captures the qualitative trend of the experiment although the model overpredicts the rotational speed. This discrepancy arises from the assumption adopted in the model. For example, the static normal force coefficient of blades taken from Kyozuka [59] in Fig. 10 is measured at $Re = \mathcal{O}(10^5)$ whereas our experiment is performed at $Re = \mathcal{O}(10^4)$. In addition, the flow is nominally two-dimensional in their experiment as the blade has end-plates on both sides, while our turbine has one end-plate on the bottom side.

$\langle TSR \rangle$ is nearly constant for all Re both in the experiment and model. At lower Reynolds numbers ($Re \lesssim 2.2 \times 10^4$), $\langle TSR \rangle$ is higher in the HT flow than in the LT flow. On average, $\langle TSR \rangle$ in the HT flow is approximately 4 % higher than that of the LT flow. At higher Re, however, the difference becomes slight. The model correctly captures this phenomenon as $\langle TSR \rangle$ is nearly the same between the steady and turbulent flows.

Fig. 13 (a) compares the time histories of TSR of the turbine obtained by the low-order model between the steady and turbulent flows at $Re = 10600$. The mean values are plotted in dash-dotted lines. The fluctuation of TSR is much greater in turbulence. PSDs of TSR in steady and turbulent flows are plotted in Fig. 13 (b). A dominant peak at the blade passing frequency $f/f_\mathrm{BP} = 1$ is clearly identified in the steady flow. Since the Savonius turbine has two

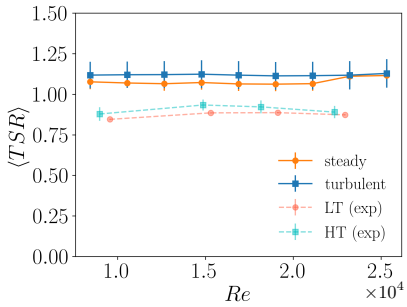

FIG. 12: The Reynolds number dependency of mean tip-speed ratio $\langle TSR \rangle$ compared between LT and HT flows. Both the experiment and model show that higher $\langle TSR \rangle$ at lower Reynolds numbers ($Re \lesssim 2.2 \times 10^4$).

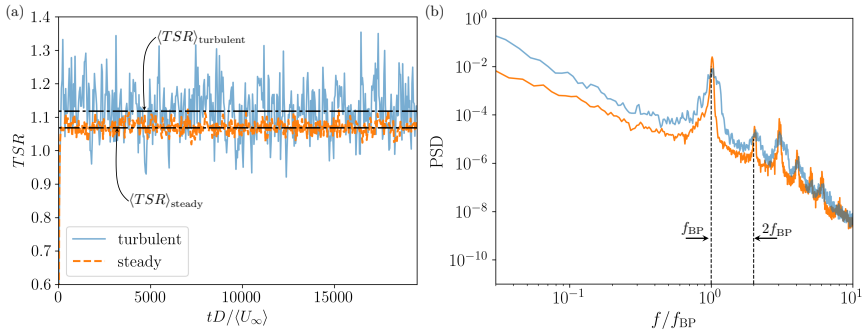

FIG. 13: (a) The comparison of the time variations of TSR of the Savonius turbine between the steady flow and the turbulent flow ($T_u = 18\%$, $L = 0.335$ m) at $Re = 10600$. Mean tip-speed ratios $\langle TSR \rangle$ are plotted in dash-dotted lines. (b) Power spectral density (PSD) of rotational speeds in the steady flow and the turbulent flow in an arbitrary unit. f_{BP} is the blade passing frequency.

blades, the blade passing frequency is twice the rotational frequency of the turbine $f_{\mathrm{BP}} = 2f_{\mathrm{rot}}$. Its harmonic peaks are also clearly identified. In turbulence, a more flattened hump is identified at $f/f_{\mathrm{BP}} = 1$. This indicates that the rotation is still relatively periodic even though the incoming flow is highly turbulent.

Fig. 14 presents the effect of turbulence intensity I_u and integral length scale L on the mean tip-speed ratio $\langle TSR \rangle$ of the turbine, predicted by the low-order model. Turbulence intensity I_u and integral length scale divided by the turbine diameter L/D are varied from 5% to 40% and from 0.1 to 10 at $Re = 10600$, respectively. It is clear that $\langle TSR \rangle$ increases with the turbulence intensity, which means that the turbulent kinetic energy of the inflow wind has a positive effect on the rotation of the turbine. At low turbulence intensity, there is not a distinct tendency in the effect of the integral length scale on $\langle TSR \rangle$. At high turbulence intensity (approximately $I_u > 35\%$), on the other hand, large integral length scales ($L/D = 10$) are harmful to the turbine rotation.

B. Savonius turbine wake

In order to investigate further the difference in the mechanism of turbine rotation between LT and HT flows, we take a look at the wake of the turbine. Fig. 15 compares the flow structure around the turbine at high azimuthal angles by smoke flow visualization. The figure presents only high azimuthal angles where the wake becomes vortex-dominated due to the separated vortex from the advancing blade. The topological flow representation of the LT flow is also depicted in the figure. In the LT flow (see Fig. 15 (a) and (b)), a flow reversal occurs in the concave side of

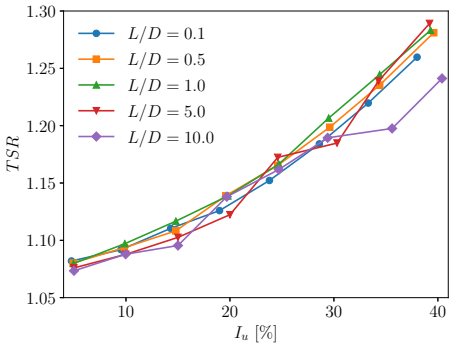

FIG. 14: The effect of turbulence intensity I_u and integral length scale L on the mean tip-speed ratio $\langle TSR \rangle$. $\langle TSR \rangle$ increases with I_u.

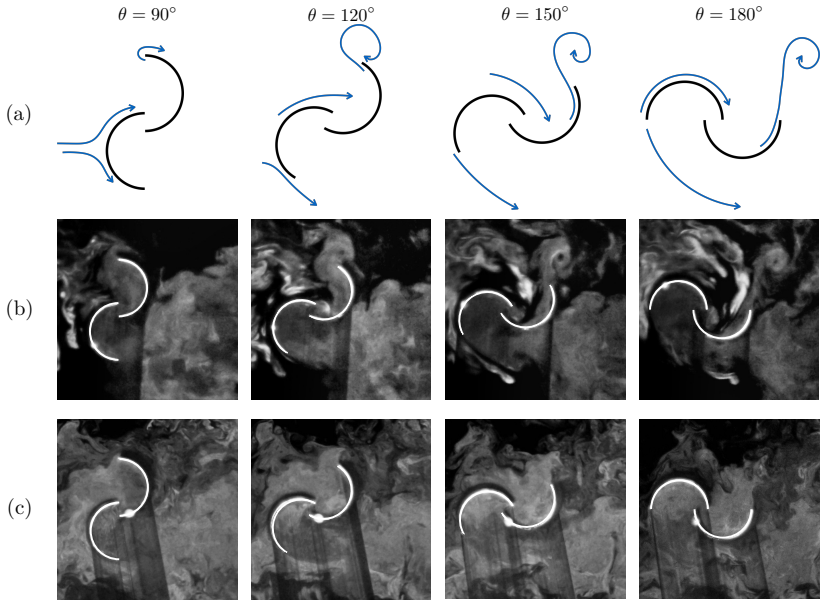

FIG. 15: Flow topology around the Savoinius turbine: (a) flow topology in the LT flow, (b) smoke flow visualization in LT flow, and (c) in the HT flow. Coherent vortex shedding is observed in the LT flow whereas the coherent vortex shedding is intermittent in the HT flow.

the advancing blade at $\theta = 90°$. This flow meets the freestream near the edge and forms a coherent vortex ($\theta = 120°$ and 150°). Subsequently, this coherent vortex is advected downstream ($\theta = 180°$). These flow structures are akin to those reported in Fujisawa [26] in which the flow around the Savonius turbine is visualised by smoke in a wind tunnel at $TSR = 0.9$, and in Nakajima *et al.* [28] where the flow is visualised by ink in water channel at $TSR = 1.1$. In the HT flow (see Fig. 15 (c)), coherent vortex shedding becomes intermittent due to high turbulence intensity. When the coherent vortex shedding is suppressed, a transition from the flow reversal to a vortex is seen at $\theta = 120°$, but this vortex does not grow into a large coherent vortex and dissipates due to the effect of freestream turbulence ($\theta = 150°$

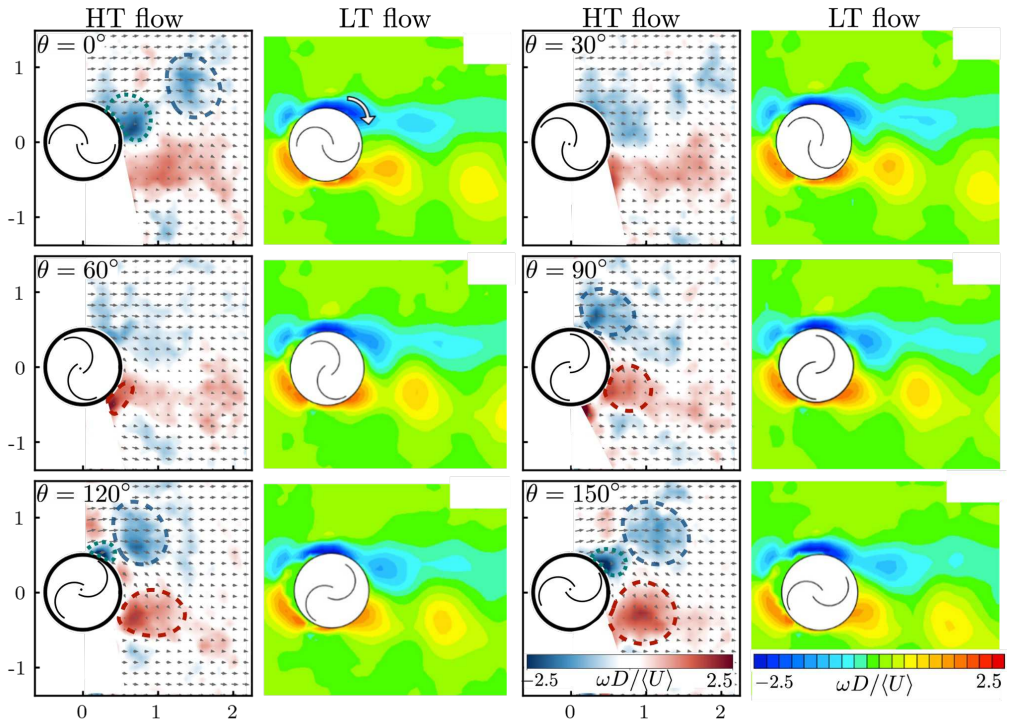

FIG. 16: The comparison of phase-averaged vorticity fields of six different rotation angles between HT and LT flows. The vorticity plots of the LT flow are taken from Shigetomi [67] in which the Savonius turbine rotates at $TSR = 0.75$ in a free-rotation condition at $Re = \mathcal{O}(10^4)$.

and 180°).

Phase-averaged vorticity is compared between the HT and LT flows in Fig. 16. The vorticity plot of the LT flow is taken from Shigetomi [67] in which the Savonius turbine of a similar geometry rotates at $TSR = 0.75$ in the unloaded (free-rotation) condition at $Re = \mathcal{O}(10^4)$, using the same wind tunnel facility. The results using the same data set are also published in [15]. Overall, the vortical structures around the turbine are similar between the HT and LT flow in the near-wake $x/D < 1$. The distinct difference appears in the far-wake $x/D > 1$, where vortical structures dissipate in the HT flow. Shed vortices from advancing and returning blades are clearly visible in the wake of the LT flow, whereas in the HT flow, such vortices spread out due to high turbulence intensity. For example, the returning blade vortex (RBV) in the HT flow starts to grow at $\theta = 60°$ as marked in the red dashed line in the figure. This RBV grows and detaches from the blade at $\theta = 120° - 150°$. At $\theta = 180°(0°)$, the RBV is not coherent anymore whereas that of the LT flow remains coherent.

It is also clear that the advancing blade vortex (ABV) growth and shedding cycle are different between the LT and HT flows. In the LT flow, the ABV begins to grow at $\theta = 60°$. The ABV grows until it detaches from the turbine in one cycle ($\theta = 90° + 180° = 270°(90°)$). In the HT flow, the ABV starts to grow at $\theta = 60°$, though it is not visible in the figure. This ABV detaches from the blade at $\theta = 90°$ and advects downstream afterwards (see the blue dashed line in Fig. 16). At $\theta = 120°$, the second ABV starts to grow (see the dotted line in dark green in the figure). However, this second ABV cannot remain as a vortex and dissipates in the wake (see $\theta = 0° - 60°$).

Another clear difference is the trajectory of the ABV. In both HT and LT flows, the ABV begins to detach from the turbine and advect downstream at $\theta = 120° - 150°$, but in the HT flow, the ABV travels in the positive $y-$direction once it detaches from the turbine (see the blue dashed line in Fig. 16) while that of the LT flows travels slightly in the

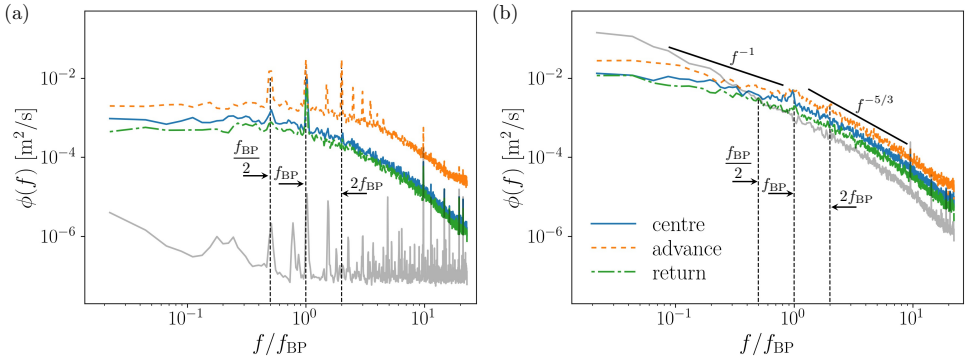

FIG. 17: Power spectral density (PSD) of velocity fluctuation measured in the wake: (a) LT flow and (b) HT flow. f_{BP} is the blade passing frequency. The spectra of the inflow velocity are shown in the grey lines. 'centre', 'advance', and 'return' denote the locations where the velocity is sampled by HWA: $1D$ behind the turbine along the centreline, $1D$ behind the advancing blade, and $1D$ behind the returning blade.

negative $y-$direction. This is because the clockwise rotation of the turbine accelerates the flow around the advancing blade in the in the negative $y-$direction in the LT flow, whereas high turbulence intensity attenuates the induced velocity in the negative $y-$direction due to the rotation of the advancing blade.

To further understand the difference in the wake between the LT and HT flows, we have a look at the power spectral densities (PSDs) of the wake velocity obtained by HWA. As already shown in Fig. 6, the hot-wire measures the wake velocity at three different positions, which are on the centreline, behind the advancing blade, and behind the returning blade at $x/D = 1$. These positions are selected because ABV and RBV pass through after they separate from the turbine and before they dissipate in the wake (see the vorticity field of LT flows in Fig. 16). Fig. 17 compares the PSDs of the wake velocity of the turbine at three different positions, between the LT flow (Fig. 17 (a)) and the HT flow (Fig. 17 (b)).

In the LT flow (Fig. 17 (a)), there are clear peaks at frequencies corresponding with the turbine's blade passing frequency $f_{BP} = 2f_{rot} = 21.97$ Hz. There are also peaks at harmonics of f_{BP} in the PSD of the advancing blade wake. On the other hand, there is also a peak at a frequency corresponding with half the blade passing frequency $0.5f_{BP} = f_{rot} = 10.98$ Hz in the PSD of the advancing blade wake in particular. This is a feature of a body that is auto-rotating perpendicular to the flow at a high tip-speed ratio $TSR > 0.5$ [15, 68, 69]. The advancing blade generally sheds a vortex every half a rotation. At a high TSR, however, the shed vortex from the advancing blade is caught up by a newly generated advancing blade vortex at around $x/D = 1$, and eventually these two advancing blade vortices merge into a single vortex [68, 69]. Therefore, the vortex shedding frequency equal to the turbine rotation frequency is observed. The PSD of the advancing blade wake exhibits much higher intensity than the other two because the wake velocity behind the advancing blade is faster due to its rotating direction.

Figure 17 (b) provides the PSD of wake velocities in the HT flow. The predominant difference from the LT flow is that there is no remarkable peak at f_{BP} regardless of wake positions. Furthermore, there are no peaks at the harmonics of f_{BP} and a half of f_{BP}. As a result, PSDs obtained at three different positions in the turbine wake have continuous spectra under the energy cascade process. A large-scale coherent vortex cannot be formed since the energy cascade process dissipates such vortices before they start growing as seen in the flowfield in Fig. 16. Intensities of PSDs at the blade passing frequency $\phi(f_{BP})$ are low compared with those in LT flows. In addition, the PSD of the advancing blade wake is almost the same as the others while that of the LT flow has much higher intensity. This result suggests that the vortex shedding due to the turbine rotation is alleviated in the HT flow. In other words, the rotation of the advancing blade does not accelerate the flow, which results in less velocity gradient and hence the attenuated ABV shedding, as observed in the flowfield in Fig. 16. Therefore, the kinetic energy that is generated by the turbine rotation and shed into the wake is attenuated and transformed into the energy available for the turbine. We deem that this is one of the reasons that improves the torque and power of the Savonius turbine in turbulence. The attenuated vortex shedding in turbulence is also reported for static bluff bodies with different geometries, such as cylinders [29], spheres [30], disks [31], and cubes [32].

To further understand the wake structure, proper orthogonal decomposition (POD) is employed to extract flow structures around the Savonius turbine in the HT flow. POD approximates the physical parameters as a linear

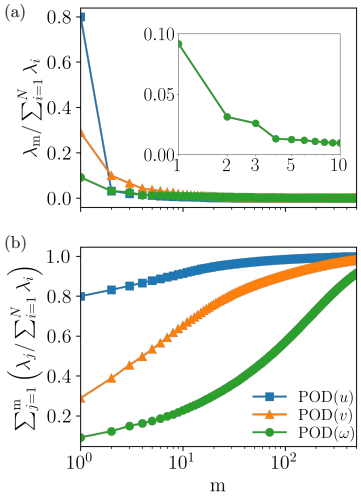

FIG. 18: (a) Eigenvalue distribution and (b) cumulative distribution of streamwise velocity u, stream-normal velocity v, and vorticity ω as a function of the number of modes m. The magnified window in (a) shows the first 10 POD modes of the vorticity ω.

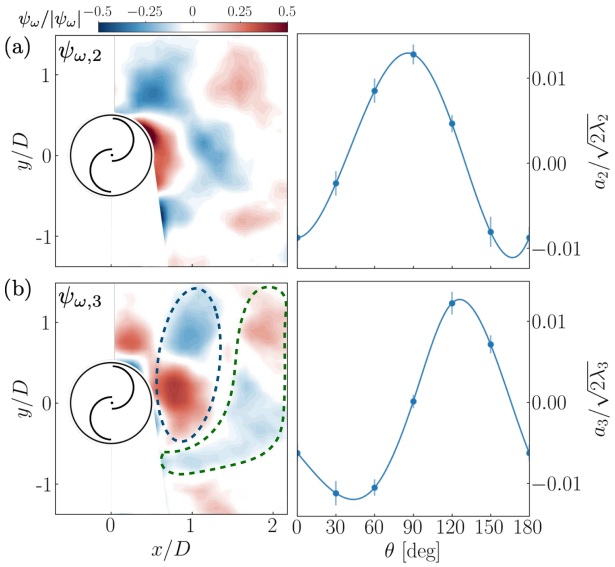

FIG. 19: (a) Second and (b) third POD modes of vorticity field and corresponding time coefficients. The blue dashed line indicates a vortex pair structure and the green dashed line indicates the Kármán vortex-like structure.

combination of spatial eigenfunctions with time coefficients. For straight-bladed VAWT, Le Fouest *et al.* [70] and Dave and Franck [71] succeeded in connecting POD modes with torque generation mechanism. Eigenvalues are sorted such that the first mode is the most dominant flow structure. Flowfields ($\mathbf{u}$, $\mathbf{v}$, $\boldsymbol{\omega}$) are reconstructed as, for example for vorticity $\boldsymbol{\omega}$

$$\boldsymbol{\omega}(x,y) = \sum_{\mathrm{i}}^{N} a_{\mathrm{i}}(t_{\mathrm{n}})\boldsymbol{\psi}_{\omega,\mathrm{i}}(x,y), \tag{13}$$

where a_{i} is the time coefficient of the i-th POD mode ψ_i. In total, 5000 PIV snapshots are used for POD, and 20 modes are used to reconstruct the instantaneous flowfields. The time coefficient a_{i} indicates the significance of i-th mode with respect to time.

The eigenvalue distribution of the first 500 POD modes is depicted in Fig. 18. The magnified window in (a) shows the first 10 POD modes of the vorticity. Although the POD modes for the streamwise and stream-normal velocities (u and v) are not shown in this paper, the eigenvalue distribution for these velocities is also plotted with that of vorticity. The second and third POD modes of vorticity dominate the rest as shown in the magnified window in Fig. 18 (a), but each has only 3% of the total energy. This means that the vortex shedding is highly intermittent and chaotic. Fig. 18 (b) shows the first 100 POD modes of vorticity represent approximately 60% of the total energy.

Figure 19 presents the second and third POD modes of vorticity field and corresponding time coefficients. The time coefficients a_{i} are normalised by the eigenvalues obtained by POD. The first mode is not presented here because it shows the time-averaged flowfields. Both the second and third modes reflect a periodic vortex shedding pattern. Furthermore, they capture coherent vortex structures in the far-wake of the turbine at $x/D = 2$, which are not captured by the phase-averaged vorticity field. The second mode mainly captures the vorticity field at $\theta = 90°$ where the time coefficient takes its maximum. By comparing this mode with the phase-averaged vorticity field shown in Fig. 16, this mode clearly captures the vortical structure near the advancing blade. Although we do not measure the time-dependent torque, this mode will probably be the torque-generating mode since the dynamic torque of a freely-rotating Savonius turbine takes its highest at around $\theta = 90°$ and the lowest at $\theta = 0°$ [13]. In addition, the second mode also captures the shed vortex from the advancing blade, shown as a red region at around $(x/D, y/D) = (2, 1)$, at $\theta = 150° - 180°$ (or 0°), where the time coefficient takes its negative peak. Note that the sign of the vorticity (red and blue in colour) is inverted in the POD mode because of the negative time coefficient (i.e. $\omega = \sum_{\mathrm{i}}^{N} a_{\mathrm{i}}(t_{\mathrm{n}})\boldsymbol{\psi}_{\omega,\mathrm{i}}$).

The time coefficient of the third mode (Fig. 19 (b)) has the positive peak at $\theta = 120° - 150°$. The mode represents the counter-rotating twin vortex behind the turbine ($x/D = 1$) that is seen from the phase-averaged vorticity field in Fig. 16. The negative peak of the time coefficient is present at $\theta = 30° - 60°$. This mode captures the Kármán vortex-like structure at $x/D = 2$, which is not identified by the phase-averaged vorticity field (c.f. Fig. 16). This Kármán vortex-like structure is the feature of the fast-rotating Savonius turbine [15].

VI. CONCLUDING REMARKS

This study reports the effect of turbulence on the rotation and the wake of the Savonius turbine at $Re = \mathcal{O}(10^4)$. We use the far-field of the open-jet where turbulence intensity is high ($I_u = 18\%$) with a wide inertial subrange following Kolmogorov's -5/3 law. As a result, we find turbulence intensity plays a significant role in the turbine rotation.

The mean tip-speed ratio $\langle TSR \rangle$ of the Savonius turbine is approximately 4% higher in the HT flow than the LT flow when the turbine receives the same mean inflow velocity. This is due to two reasons. One is the turbulence intensity, which theoretically increases the time-averaged torque and power of the turbine. The other is the attenuated vortex shedding due to turbulence. The effect of turbulence intensity is confirmed by developing a low-order model to predict the flow-induced rotation of the turbine. We find that the turbulence intensity particularly augments TSR, which corroborates our experimental results. In addition, we also find that TSR is increased when the scale of turbulence (the integral scale) has a similar size as the Savonius turbine.

The attenuated vortex shedding is confirmed by PIV and HWA. PIV shows that the vortex shedding in the HT flow is attenuated so coherent vortical structures are not clearly formed. HWA reveals that any peaks in PSDs of the wake velocities corresponding with the blade passing frequency f_{BP} and its harmonics are not observed in the HT flow, while remarkable peaks are identified in the LT flow. Finally, the POD analysis confirms that the vortex shedding process is highly intermittent. Nonetheless, the first two modes, which have approximately 3% of the total energy each, capture coherent vortex structures that are not seen in the phase-averaged vorticity field. These results indicate that the vortex shedding process (kinetic energy loss into wake) due to the turbine rotation is attenuated because of the highly turbulent inflow.

The present study experimentally and analytically provides the future possibilities that the Savonius wind turbine will be more commonplace in urban areas due to its robustness with turbulence, as well as its well-known advantages such as quiet operations. The results may not only be relevant to Savonius turbines but also any kind of turbines that are exposed to high turbulence intensity with Kolmogorov energy cascade.

Meanwhile, this study also suggests that the current process of wind turbine design assuming steady and uniform flows without considering turbulence can overlook its significant features. The present study provides the results of the unloaded free-rotation at $Re = \mathcal{O}(10^4)$ under the hypothesis that the change in torque would appear in the free rotational speed. Nonetheless, torque measurement for a passively rotating Savonius turbine at different TSR will be desired to strengthen this hypothesis. Further, future studies should be performed to investigate the effect of turbulence intensity on the torque and power of the Savonius turbine. In future work, therefore, we will conduct time-resolved torque measurements at different tip-speed ratios to characterise more detailed torque and power differences over a range of turbulence intensities.

ACKNOWLEDGMENTS

This research is supported by Japan Society for the Promotion of Science (Grant No.15K13861). The authors express their gratitude to technician emeritus Mr Toshiyuki Sampo for his assistance in the construction of our experimental apparatus. The authors would like to thank the four anonymous reviewers whose feedback substantially helped improve the quality of this manuscript.

AUTHOR CONTRIBUTIONS

S. Ōtomo: Methodology, Software, Formal analysis, Experiments, Modelling, Visualisation, Original Draft, Writing; **Y. Tasaka**: Supervision, Conceptualisation, Writing; **P. Denissenko**: Supervision, Conceptualisation, Writing; **Y. Murai**: Supervision, Conceptualisation, Funding acquisition, Writing.

[1] F. Toja-Silva, A. Colmenar-Santos, and M. Castro-Gil, Renewable and Sustainable Energy Reviews **24**, 364 (2013).
[2] T. Ishugah, Y. Li, R. Wang, and J. Kiplagat, Renewable and Sustainable Energy Reviews **37**, 613 (2014).
[3] F. Emejeamara, A. Tomlin, and J. Millward-Hopkins, Renewable Energy **81**, 162 (2015).
[4] S. J. Savonius, *The wing-rotor in theory and practice* (Omnia-Mikrofilm-Technik, 1981).
[5] J. Zou, Y. Yu, J. Liu, J. Niu, K. Chauhan, and C. Lei, Building and Environment **194**, 107713 (2021).
[6] R. Ricci, R. Romagnoli, S. Montelpare, and D. Vitali, Applied Energy **161**, 143 (2016).
[7] S. Montelpare, V. D'Alessandro, A. Zoppi, and R. Ricci, Energy **144**, 146 (2018).
[8] Y. Jooss, R. Bolis, T. Bracchi, and R. J. Hearst, Flow **2**, E10 (2022).
[9] Y. Jooss, E. B. Rønning, R. J. Hearst, and T. Bracchi, Journal of Wind Engineering and Industrial Aerodynamics **230**, 105177 (2022).
[10] Y. Jooss, R. J. Hearst, and T. Bracchi, Journal of Renewable and Sustainable Energy **15** (2023), 10.1063/5.0170059.
[11] A. Damak, Z. Driss, and M. Abid, Renewable Energy **52**, 136 (2013).
[12] B. Blackwell, R. Sheldahl, and L. Feltz, *Wind tunnel performance data for two-and three-bucket Savonius rotors* (Sandia Laboratories, 1977).
[13] L. Wang and R. W. Yeung, Applied Energy **183**, 823 (2016).
[14] New World Wind, "Aeroleaf®," `https://newworldwind.com/aeroleaf`, accessed: (08.09.2023).
[15] A. Shigetomi, Y. Murai, Y. Tasaka, and Y. Takeda, Renewable Energy **36**, 536 (2011).
[16] W. Tian, A. Ozbay, and H. Hu, Physics of Fluids **26**, 125108 (2014).
[17] W. Lubitz, Renewable Energy **61**, 69 (2014).
[18] D. Wekesa, C. Wang, Y. Wei, and W. Zhu, Journal of Wind Engineering and Industrial Aerodynamics **157**, 1 (2016).
[19] S. Rockel, J. Peinke, M. Hölling, and R. B. Cal, Renewable Energy **112**, 1 (2017).
[20] M. Talavera and F. Shu, Renewable Energy **109**, 363 (2017).
[21] W. Tian, A. Ozbay, and H. Hu, Journal of Fluids and Structures **85**, 17 (2019).
[22] A. Vinod and A. Banerjee, Applied energy **254**, 113639 (2019).
[23] S. Gambuzza and B. Ganapathisubramani, Journal of Renewable and Sustainable Energy **13** (2021), 10.1063/5.0039168.
[24] B. Loganathan, I. Mustary, H. Chowdhury, and F. Alam, Energy Procedia **110**, 549 (2017).
[25] A. D. Aliferis, M. S. Jessen, T. Bracchi, and R. J. Hearst, Wind Energy (2019), 10.1002/we.2358.
[26] N. Fujisawa, Journal of Wind Engineering and Industrial Aerodynamics **40**, 277 (1992).
[27] Y. Murai, T. Nakada, T. Suzuki, and F. Yamamoto, Measurement Science and Technology **18**, 2491 (2007).
[28] M. Nakajima, S. Iio, and T. Ikeda, Journal of Fluid Science and Technology **3**, 420 (2008).

[29] H. Blackburn and W. Melbourne, Journal of Fluid Mechanics **306**, 267 (1996).
[30] H. Tyagi, R. Liu, D. S.-K. Ting, and C. R. Johnston, Experimental thermal and fluid science **30**, 587 (2006).
[31] E. Rind and I. P. Castro, Experiments in fluids **53**, 301 (2012).
[32] R. J. Hearst, G. Gomit, and B. Ganapathisubramani, Journal of Fluid Mechanics **804**, 513 (2016).
[33] L. Chen, J. Chen, and Z. Zhang, Journal of Renewable and Sustainable Energy **10**, 013306 (2018).
[34] M. Gibson, Journal of Fluid Mechanics **15**, 161 (1963).
[35] F. Champagne, Journal of Fluid Mechanics **86**, 67 (1978).
[36] P. Burattini, R. Antonia, and L. Danaila, Physics of Fluids **17**, 025101 (2005).
[37] A. Ghasemi, V. Roussinova, and R. Balachandar, Journal of Turbulence **14**, 1 (2013).
[38] B. Pani and R. Dash, Journal of Hydraulic Engineering **109**, 254 (1983).
[39] N. Rajaratnam, *Turbulent Jets* (Elsevier, 1976).
[40] M. Xu, A. Pollard, J. Mi, F. Secretain, and H. Sadeghi, Physics of Fluids **25**, 035102 (2013).
[41] J. Mi and G. Nathan, Flow, Turbulence and Combustion **84**, 583 (2010).
[42] M. Xu, J. Zhang, P. Li, and J. Mi, Theoretical and Applied Mechanics Letters **5**, 117 (2015).
[43] G. Batchelor, *The theory of homogeneous turbulence* (Cambridge university press, 1953).
[44] A. Kistler and T. Vrebalovich, Journal of Fluid Mechanics **26**, 37 (1966).
[45] C. Sicot, P. Devinant, T. Laverne, S. Loyer, and J. Hureau, Wind energy **9**, 361 (2006).
[46] C.-R. Chu and P.-H. Chiang, Journal of Wind Engineering and Industrial Aerodynamics **124**, 82 (2014).
[47] M. Gad-el-Hak and S. Corrsin, Journal of Fluid Mechanics **62**, 115 (1974).
[48] H. Makita, Fluid Dynamics Research **8**, 53 (1991).
[49] A. Praskovsky and S. Oncley, Physics of Fluids **6**, 2886 (1994).
[50] P. Welch, IEEE Transactions on audio and electroacoustics **15**, 70 (1967).
[51] A. Kumar and R. P. Saini, Renewable and Sustainable Energy Reviews **64**, 289 (2016).
[52] O. d. Vries, *Fluid dynamic aspects of wind energy conversion*, Tech. Rep. (Advisory Group for Aerospace Research and Development NEUILLY-SUR-SEINE (France), 1979).
[53] R. Wagner, I. Antoniou, S. M. Pedersen, M. S. Courtney, and H. E. Jørgensen, Wind Energy: An International Journal for Progress and Applications in Wind Power Conversion Technology **12**, 348 (2009).
[54] R. Wagner, M. Courtney, J. Gottschall, and P. Lindelöw-Marsden, Wind Energy **14**, 993 (2011).
[55] A. Choukulkar, Y. Pichugina, C. T. Clack, R. Calhoun, R. Banta, A. Brewer, and M. Hardesty, Wind Energy **19**, 1439 (2016).
[56] J. Westerweel and F. Scarano, Experiments in Fluids **39**, 1096 (2005).
[57] T. Ido, Y. Murai, and F. Yamamoto, Experiments in Fluids **32**, 326 (2002).
[58] T. Ido and Y. Murai, Flow Measurement and Instrumentation **17**, 267 (2006).
[59] Y. Kyozuka, Journal of Fluid Science and Technology **3**, 439 (2008).
[60] M. Shinozuka, Computers & Structures **2**, 855 (1972).
[61] M. Shinozuka, C.-B. Yun, and H. Seya, Journal of Wind Engineering and Industrial Aerodynamics **36**, 829 (1990).
[62] G. T. Scarlett and I. M. Viola, Renewable Energy **146**, 843 (2020).
[63] T. von Kármán, Proceedings of the National Academy of Sciences of the United States of America **34**, 530 (1948).
[64] J. Kaimal, J. Wyngaard, Y. Izumi, and O. Coté, Quarterly Journal of the Royal Meteorological Society **98**, 563 (1972).
[65] J. F. Manwell, J. G. McGowan, and A. L. Rogers, *Wind energy explained: theory, design and application* (John Wiley & Sons, 2010).
[66] T. Burton, N. Jenkins, D. Sharpe, and E. Bossanyi, *Wind energy handbook* (John Wiley & Sons, 2011).
[67] A. Shigetomi, "Interacting flow field in two savonius turbines system," (2010).
[68] Y. Suzuki, M. Kiya, and T. Takahashi, Transactions of Japanese Society of Mechanical Engineers, Series B **52**, 3898 (1986), [in Japanese].
[69] M. Yamagishi, Journal of the Visualization Society of Japan **24**, 79 (2004), [in Japanese].
[70] S. Le Fouest, D. Fernex, and K. Mulleners, Flow **3**, E11 (2023).
[71] M. Dave and J. A. Franck, Physical Review Fluids **8**, 074702 (2023).